

# Ag<sub>2</sub>S Biocompatible Ensembles as Dual OCT Contrast Agents and NIR Ocular Imaging Probes

Amalia Coro, Ada Herrero Ruiz, Mateo Pazo-González, Alonso Sánchez-Cruz, Tobias Busch, Alejandro Hernández Medel, Erving C. Ximendes, Dirk H. Ortgies, Rosalía López-Méndez, Ana Espinosa, Dorleta Jimenez de Aberasturi, Daniel Jaque, Nuria Fernández Monsalve, Enrique J. de la Rosa, Catalina Hernández-Sánchez, Emma Martín Rodríguez,\* and Beatriz H. Juárez\*

Ag<sub>2</sub>S nanoparticles (NPs) emerge as a unique system that simultaneously features in vivo near-infrared (NIR) imaging, remote heating, and low toxicity thermal sensing. In this work, their capabilities are extended into the fields of optical coherence tomography (OCT), as contrast agents, and NIR probes in both ex vivo and in vivo experiments in eyeballs. The new dual property for ocular imaging is obtained by the preparation of Ag<sub>2</sub>S NPs ensembles with a biocompatible amphiphilic block copolymer. Rather than a classical ligand exchange, where surface traps may arise due to incomplete replacement of surface sites, the use of this polymer provides a protective extra layer that preserves the photoluminescence properties of the NPs, and the procedure allows for the controlled preparation of submicrometric scattering centers. The resulting NPs ensembles show extraordinary colloidal stability with time and biocompatibility, enhancing the contrast in OCT with simultaneous NIR imaging in the second biological window.

## 1. Introduction

Colloidal Ag<sub>2</sub>S NPs have emerged as ideal systems in nanomedicine combining synergetic capabilities including near-infrared (NIR) imaging, photothermal heating, and nanothermometry.<sup>[1]</sup> These capabilities are the result of their optical properties, which can be tuned through straightforward synthetic routes that allow obtaining NPs with controlled size, narrow size distribution, good biocompatibility, and high stability over time. With a bulk band gap energy of 1.1 eV for monoclinic  $\alpha$ -Ag<sub>2</sub>S, Ag<sub>2</sub>S NPs can be excited within the first biological window and emit photoluminescence (PL) at the second, in particular around 1200 nm for NP sizes above 4 nm, out of

A. Coro, A. Espinosa, B. H. Juárez  
Instituto de Ciencia de Materiales de Madrid  
CSIC  
C/ Sor Juana Inés de la Cruz, 3, 28049 Madrid, Spain  
E-mail: bh.juarez@csic.es

A. Herrero Ruiz, D. Jimenez de Aberasturi  
CiCbiomaGUNE  
Basque Research and Technology Alliance (BRTA)  
Miramon Pasealekua, 182, 20014 Donostia-San Sebastián,  
Gipuzkoa, Spain

A. Herrero Ruiz, D. Jimenez de Aberasturi  
Centro de Investigación Biomédica en Red de Bioingeniería,  
Biomateriales y, Nanomedicina (CIBER-BBN)  
20014 Donostia-San Sebastián, Spain

M. Pazo-González, A. Sánchez-Cruz, E. J. de la Rosa,  
C. Hernández-Sánchez  
Centro de Investigaciones Biológicas Margarita Salas  
CSIC  
C/ Ramiro de Maeztu, 9, 28040 Madrid, Spain

M. Pazo-González  
Department of Systems Biology, Facultad de Medicina  
Universidad de Alcalá  
Ctra de Madrid-Barcelona, Km 33,600 Alcalá de Henares,  
28871 Madrid, Spain

M. Pazo-González  
Visual Neurophysiology Group  
Instituto Ramón y Cajal de Investigación Sanitaria (IRYCIS)  
Ctra. Colmenar Viejo, km. 9, 100, 28034 Madrid, Spain

T. Busch, A. Hernández Medel, E. C. Ximendes, D. H. Ortgies, D. Jaque,  
E. Martín Rodríguez  
Nanomaterials for Biomedicine Group (nanoBIG)  
Facultad de Ciencias  
Universidad Autónoma de Madrid  
C/ Francisco Tomás y Valiente 7, 28049 Madrid, Spain  
E-mail: emma.martin@uam.es

T. Busch, A. Hernández Medel, E. C. Ximendes, D. H. Ortgies, D. Jaque,  
N. Fernández Monsalve, E. Martín Rodríguez  
Instituto Ramón y Cajal de Investigación Sanitaria (IRYCIS)  
Ctra. Colmenar Viejo, km. 9, 100, 28034 Madrid, Spain

The ORCID identification number(s) for the author(s) of this article can be found under <https://doi.org/10.1002/sml.202305026>

© 2023 The Authors. Small published by Wiley-VCH GmbH. This is an open access article under the terms of the Creative Commons Attribution-NonCommercial-NoDerivs License, which permits use and distribution in any medium, provided the original work is properly cited, the use is non-commercial and no modifications or adaptations are made.

DOI: 10.1002/sml.202305026

quantum confinement.<sup>[2]</sup> This property enables bright NIR imaging<sup>[3]</sup> and, for example, NIR-guided surgery with a threefold reduction in the residual tumoral cells after a tumor resection.<sup>[4]</sup> Ag<sub>2</sub>S NPs have also been used as excellent nanothermometers, probes to measure temperature variations in biological systems with high thermal sensitivity in localized areas.<sup>[5]</sup> This capability arises from the dependence of PL of NPs on temperature, and has enabled their use as precise diagnostic tools for the early detection of solid tumors,<sup>[6]</sup> ischemic, infarcted, and/or inflamed tissues.<sup>[7,8]</sup> Furthermore, Ag<sub>2</sub>S NPs have been used to measure in vivo temperature variations in a mouse brain<sup>[9]</sup> and mouse liver,<sup>[10]</sup> and to register temperature variations during an in vivo magnetic hyperthermia treatment with maghemite-Ag<sub>2</sub>S nanoplateforms.<sup>[11]</sup>

Out of the numerous recipes reported for colloidal synthesis of Ag<sub>2</sub>S NPs,<sup>[1]</sup> one of the most-employed recipes includes the thermal decomposition of silver(I) diethyldithiocarbamate (AgDDTC), a route that yields no individual NPs but NPs organized in ordered arrangements that show poor colloidal stability in non-polar organic solvents.<sup>[12]</sup> The formation of these micrometer-sized arrangements has been considered detrimental for further treatments and applications, where stable colloidal dispersions containing individual NPs are sought. To avoid that limitation, many other recipes have been reported.<sup>[13–17]</sup> We reported an alternative procedure based on a hot-injection method that yields monodisperse individual NPs, which can be further covered with additional layers to improve their brightness. Furthermore, this enables straightforward ligand exchange reactions to transfer the NPs to aqueous media.<sup>[18]</sup> In comparison, other strategies apply post-sonication treatments to unbundle the assemblies.<sup>[19]</sup> However, submicrometric Ag<sub>2</sub>S arrangements show advantages that render them ideal dual probes as contrast agents for optical coherence tomography (OCT) and NIR PL imaging.

OCT is an optical imaging technique that is widely used for diagnosis in fields such as dermatology, cardiology, and ophthalmology. It is an interferometric method based on multiple scattering of light in tissues that allows reconstruction of their morphology with micrometric resolution. To obtain higher contrast, NPs or, in general, systems capable of increasing the scattered light have been used as contrast agents for OCT. Ideal contrast agents for OCT rely on several characteristics such as high molar extinction coefficients (preferably in the NIR biological windows), high photostability, and high biocompatibility, among others.<sup>[20,21]</sup> In the case of metallic NPs, localized surface plasmon resonances guarantee many of these requirements.<sup>[22]</sup> However, other materials such as sub-micrometric polymeric colloids<sup>[23]</sup> as well as other semiconductor materials such as CuS,<sup>[24]</sup> PbS,<sup>[25]</sup> or Bi<sub>2</sub>S<sub>3</sub> NPs<sup>[26]</sup> show excellent properties that help to better discern biological features.

On the other hand, ocular NIR imaging is attained by mainly, i) the reflectance of NIR light from the ocular fundus, which allows the following up of many conditions, including ocular inflammatory or vascular diseases, with high resolution,<sup>[27]</sup> and ii) by the use of fluorophore dyes, being the most common indocyanine green, a dye that suffers from rapid photodegradation. Recently, more robust triazole cyanine dyes have been proposed.<sup>[28]</sup> In this work, NIR imaging is performed based on the PL signal of biocompatibilized Ag<sub>2</sub>S NPs intravitreally injected in mice eyes, which allows acquiring high resolution images with a NIR camera.

Ag<sub>2</sub>S NPs produced in organic media can be biocompatibilized by ligand exchange reactions of the initial ligands, which are replaced by, typically, biocompatible polyethylene glycol-based ligands.<sup>[29,30]</sup> However, it is well known that these reactions usually yield a substantial drop in PL emission (and eventually brightness) due to an incomplete passivation of the surface, partially derived from steric hindrance restricting the complete exchange. Other well-known approaches to biocompatibilize NPs include the encapsulation of as-prepared NPs with amphiphilic polymers, a pathway for the transfer of semiconductor, magnetic, metallic, and up-converting nanoparticles from nonpolar to polar environments.<sup>[30]</sup>

To mitigate these issues, we propose the strategy of synthesizing Ag<sub>2</sub>S-NP ensembles that are further biocompatibilized with dodecylamine-modified poly(isobutylene-*alt*-maleic anhydride) (N-PMA), an amphiphilic block copolymer that relies on the maleic anhydride coupling with the primary amine.<sup>[31]</sup> The rationale being that, since N-PMA has evidenced its protective role for several magnetic,<sup>[32]</sup> quantum dots<sup>[33]</sup> and metallic NPs,<sup>[34]</sup> preserving their structural and optical properties, it could also be used to protect Ag<sub>2</sub>S NPs. Additionally, N-PMA has also demonstrated effective suppression of the release of toxic Ag<sup>+</sup> ions in metallic NPs,<sup>[35]</sup> which directly influence their biocompatibility. However, to the best of our knowledge, N-PMA has never been used to protect Ag<sub>2</sub>S NPs. In this work we evidence, by proton magnetic resonance spectroscopy (<sup>1</sup>H-NMR) studies including nuclear Overhauser effect spectroscopy (NOESY) analysis, the interaction of the copolymer with the ligand shell. This interaction confers Ag<sub>2</sub>S NPs high biocompatibility and retention of the photoluminescence quantum yield (PLQY). Overall, the controlled ensembles show a clearly improved OCT signal in both explanted organs (eyeballs) and in in vivo experiments

E. C. Ximendes, D. H. Ortgies, D. Jaque, E. Martín Rodríguez  
Institute for Advanced Research in Chemistry (IAdChem)  
Campus de Cantoblanco  
28049 Madrid, Spain

D. H. Ortgies, E. Martín Rodríguez  
Instituto Nicolás Cabrera  
Facultad de Ciencias  
Universidad Autónoma de Madrid  
C/ Francisco Tomás y Valiente 7, 28049 Madrid, Spain

R. López-Méndez  
Instituto IMDEA Nanociencia  
C/ Faraday, 9, 28049 Madrid, Spain

D. Jimenez de Aberasturi  
Ikerbasque  
Basque Foundation for Science  
48009 Bilbao, Spain

N. Fernández Monsalve  
nanoBIG Group  
Facultad de Medicina  
Universidad Autónoma de Madrid  
C/ Arzobispo Morcillo, 4, 28029 Madrid, Spain

C. Hernández-Sánchez  
Centro de Investigación Biomédica en Red de Diabetes y Enfermedades Metabólicas Asociadas (CIBERDEM)  
ISCIII  
28034 Madrid, Spain

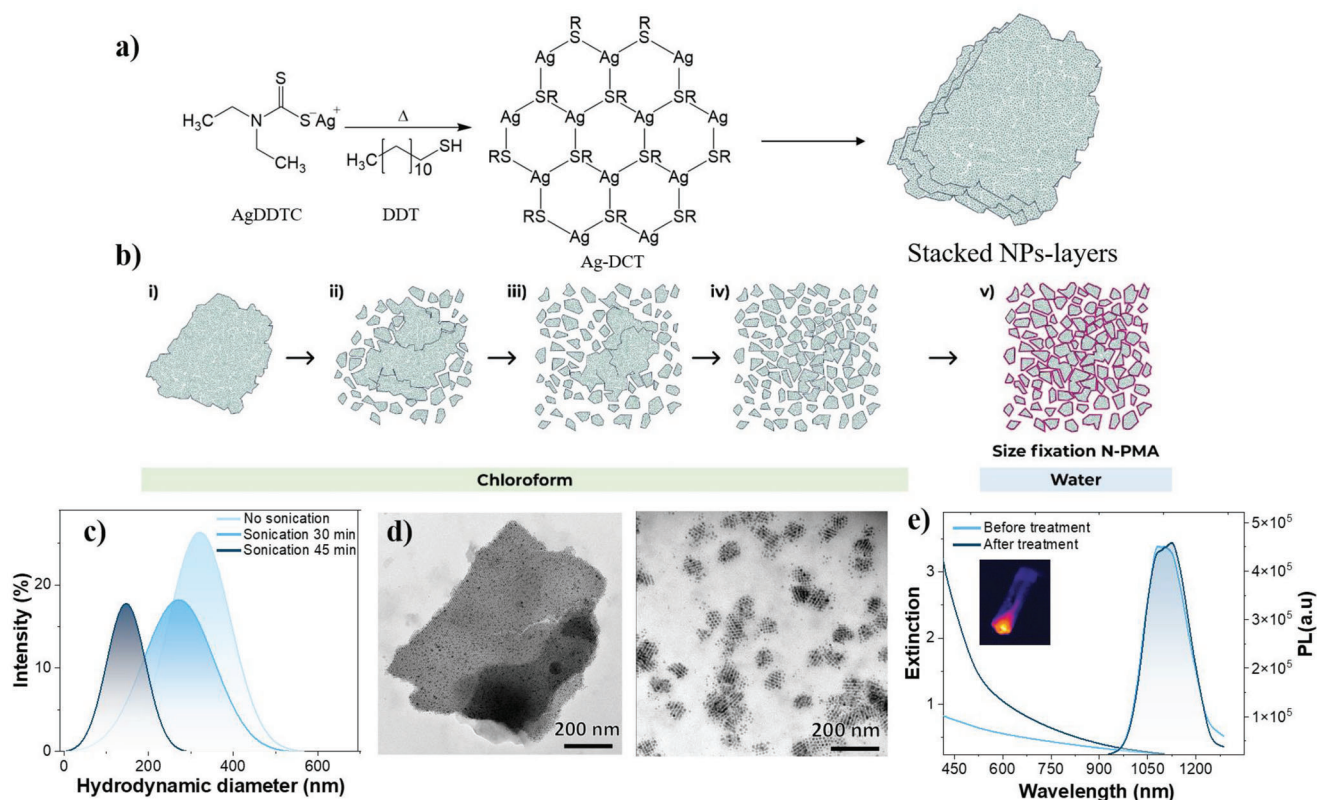


**Figure 1.** a) Sketch of the reaction of the silver precursor (AgDDTC) in DDT that includes the formation of an intermediate product (Ag-DCT) and the formation of  $\text{Ag}_2\text{S}$  NPs in stacked NP layers, (R in Ag-DCT stands for dodecyl). b) Schematic representation of the proposed mechanism for controlled ensembles formation that includes sonication in chloroform (steps ii–iv) and a last step (v) of size fixation by the treatment with N-PMA (water). c) DLS experiment measuring the size of the initial ensembles (light blue) and after sonication in chloroform after 30- (blue) and 45-min (dark blue). d) TEM images of ensembles of different sizes in water after fixation with N-PMA. e) Extinction and emission spectra of the NPs before (light blue) and after the treatment with N-PMA (dark blue). The inset shows a NIR image of a vial containing NPs upon optical excitation with an 808 nm laser diode.

performed in mice, while allowing parallel high resolution NIR imaging. Thus, N-PMA modified  $\text{Ag}_2\text{S}$  NPs are proposed as alternative dual probes for in vivo ocular imaging.

## 2. Results

### 2.1. Synthesis of $\text{Ag}_2\text{S}$ Multimodal Contrast Agents

The synthesis of the  $\text{Ag}_2\text{S}$  ensembles begins with a careful consideration of the precursor (see Section S1, Supporting Information). **Figure 1a** depicts the heat-up reaction from the Ag precursor, silver (I) diethyldithiocarbamate (AgDDTC) that, in the presence of 1-dodecanethiol (DDT), yields silver (I) dodecanethiolate (Ag-DCT), a product generated during the course of the reaction, which further passivates the surface of  $\text{Ag}_2\text{S}$  NPs, as we previously reported.<sup>[18]</sup> In fact, this layered product<sup>[36]</sup> acts as a template for the growth of the initial  $\text{Ag}_2\text{S}$  nuclei, keeping the NPs organized in laminar structures as sketched in **Figure 1a**. We reported that nucleation of  $\text{Ag}_2\text{S}$  NPs by hot injection in toluene provides isolated NPs, as hot toluene dissolves the Ag-DCT in situ.<sup>[18]</sup> However, the use of toluene limits the reaction temperature to 100 °C, producing less bright NPs than those synthesized at 200 °C.<sup>[37]</sup> The procedure reported here enables the fragmentation of the initial stacked layers to form controlled ensembles that

are soluble in water. The proposed mechanism is schematized in **Figure 1b** and proceeds with an initial exfoliation and further dissociation of NPs layers by sonication in chloroform ( $\text{CHCl}_3$ ). Depending on the sonication time, ensembles of different sizes are formed (see Section S2, Supporting Information). We have observed that the initial hydrodynamic size of the as-synthesized aggregates drops to approximately one half after 45–60 min of sonication (see **Figure S1**, Supporting Information). The final step is crucial and aims to fix the ensemble size and transfer it to aqueous media. If samples are stored in  $\text{CHCl}_3$  in the fridge for long time (months) without any fixation step, the NPs continue to disaggregate from the initial stacked layers until forming a network of slightly connected NPs (see **Figure S2** and Section S2, Supporting Information for details). Thus, the fixation of the ensembles must be done right away after the sonication procedure. The size fixation and water transfer are performed by using N-PMA (see Section S2, Supporting Information), and enable to obtain ensembles of different sizes, as can be seen in the dynamic light scattering (DLS) measurements and transmission electron microscopy (TEM) images, shown in **Figure 1c** and **d**, respectively. Further TEM images can be found in **Figure S3**, Supporting Information. The DLS measurements in **Figure 1c** correspond to the final size of the ensembles transferred to water. The ensembles were either initially non-sonicated (light blue) or

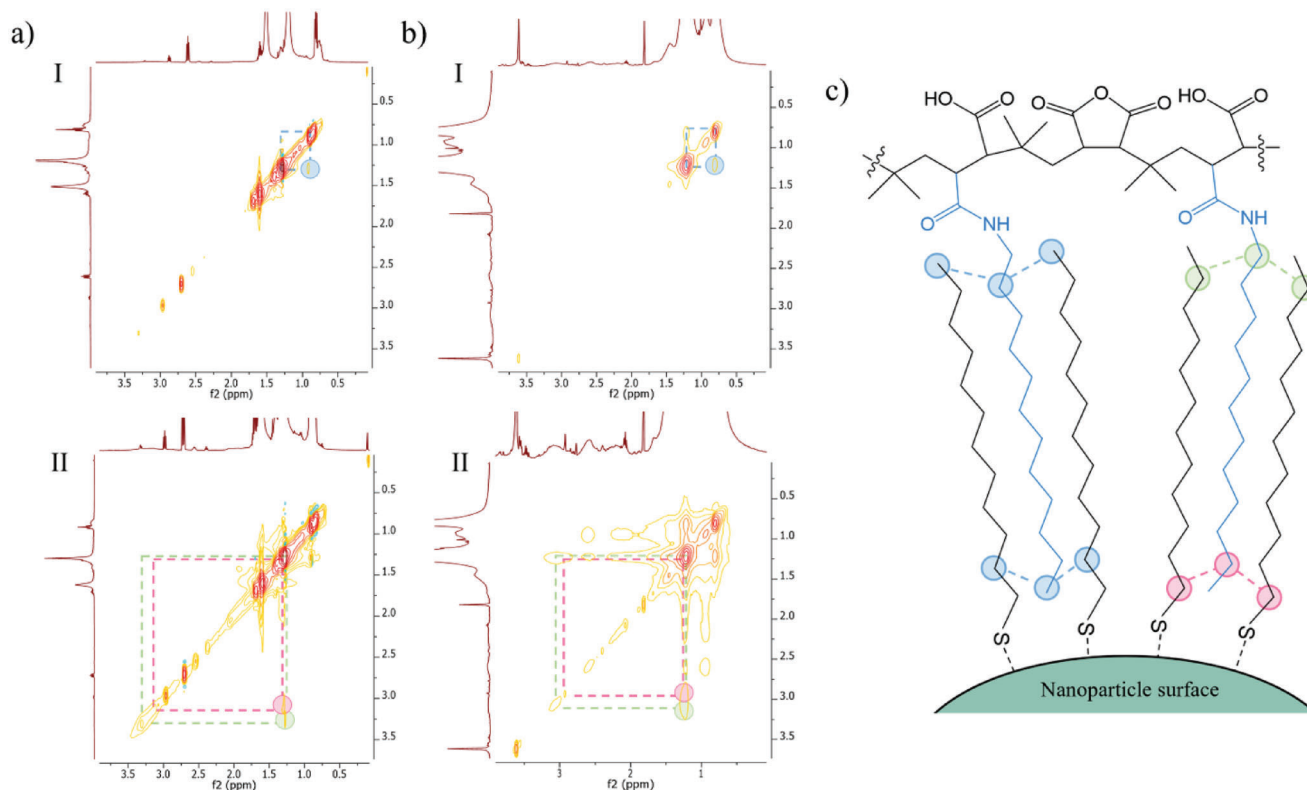


**Figure 2.** NOESY spectra in a) CDCl<sub>3</sub> and b) D<sub>2</sub>O at different signal intensities. I) Low intensity for observing the most frequent interaction and II) high intensity for detecting less frequent interactions. The image in c) indicates the corresponding interactions.

sonicated previously to the water transfer for 30 min (blue, middle) or 45 min (navy, dark blue), respectively. Furthermore, in order to evaluate the quality of samples over time, the average hydrodynamic size, polydispersity index (PI), and zeta potential (ZP) of the Ag<sub>2</sub>S NPs ensembles treated with N-PMA have been studied after 8 months. The results are shown in Figure S4 and Table S1, Supporting Information, and confirm the stability of the colloids after that time. Figure 1e shows the extinction spectrum of Ag<sub>2</sub>S NP and PL emission before (light blue) and after being treated with N-PMA (dark blue), and the inset corresponds to an NIR image of NPs dispersion upon excitation with an 808 nm laser. The as-prepared plain Ag<sub>2</sub>S NPs present an absolute PLQY, (measured in an integrating sphere) of 2.5%.<sup>[18]</sup> As can be observed, after the treatment with N-PMA, the PL emission remains constant, with no loss of the initial PL intensity, which results in an extraordinary colloidal NP-system for NIR imaging. Thus, it is clear that the high retention of the PL properties of the NPs must be related to the interaction of the NPs ligands and the hydrophobic N-PMA chain.

To analyze the ligands on the surface of the NPs and to elucidate the interaction responsible for the preservation of PLQY after the treatment with N-PMA, a detailed NMR study has been performed (experimental details in Section S3, Supporting Information). Initially, <sup>1</sup>H-NMR characterization of free ligands and surface bound ligands was recorded, as shown in Figure S5, Supporting Information, where it is evidenced that both Ag-DCT and N-PMA are detected in the stable colloidal NPs solution. To analyze the interactions between them, the structural details

of the NPs were examined using NOESY (see Figure 2), an effective technique capable of identifying the relative spatial arrangement of ligands and molecules on the surface and regularly used to discriminate between bound anchored or free ligands on NP surfaces.<sup>[36]</sup> This 2D NMR technique applies the Nuclear Overhauser Effect (NOE) to detect spin coupling between nuclei through spatial proximity (<5 Å distance), allowing in this case the study of the configuration of molecules in proximity but not covalently bound.

The NOE occurs when the irradiation of a nearby nucleus causes a transfer of energy during nuclear relaxation, resulting in a stronger signal in the magnetic resonance of nearby nuclei. In this work, we applied NOESY spectroscopy to verify the spatial organization between N-PMA and Ag-DCT-functionalized NPs.

The NOESY spectra were acquired both in CDCl<sub>3</sub> (Figure 2a) and D<sub>2</sub>O (Figure 2b), and are shown at different signal intensities (I and II, being I less intense than II). From the diagonal profiles of the spectra in Figure 2, it can be observed that there are apparent polarization interactions between both ligands (N-PMA and Ag-DCT), being more noticeable in the experiment carried out in D<sub>2</sub>O (Figure 2b), probably due to the arrangement of the hydrophobic components. Observed cross peak signals suggest intermolecular interactions between the ligands. Among them, the signals in blue circles (Figure 2 aI, bI) mainly demonstrate the interaction between the methyl protons of Ag-DCT and the methylene protons of the aliphatic chain of N-PMA. Moreover, interactions between the methylene protons of Ag-DCT and the methyl protons of N-PMA are also observed in this spectral region (see



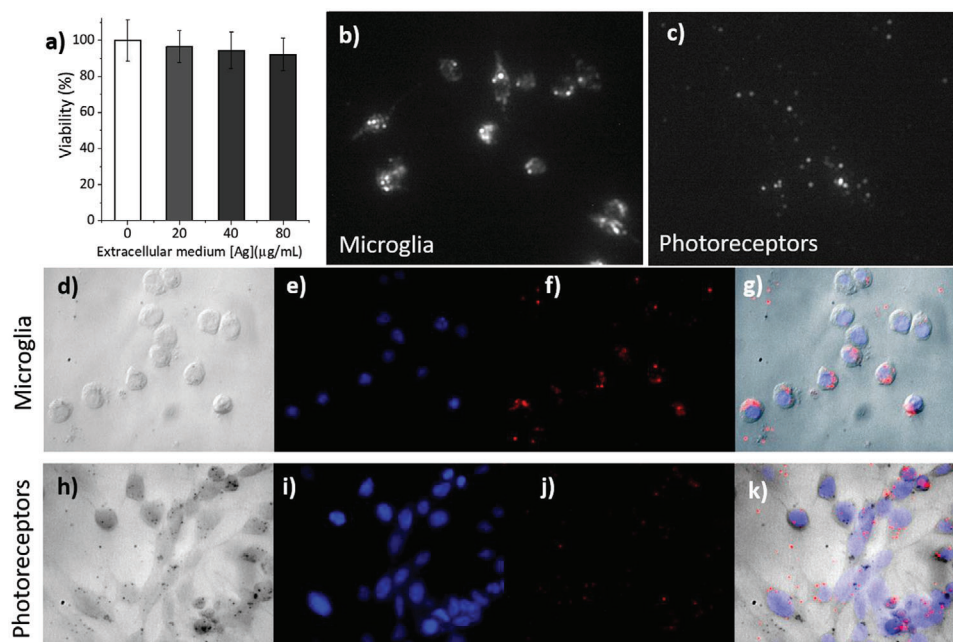


**Figure 3.** a) Viability test in N9 cells after 24 h treatment with the indicated NP concentrations in the extracellular medium- Graph shows mean  $\pm$  SD ( $n = 3$ ). b–k). Representative images of b,d–g) N9 microglia cell line and c,h–k) 661 w photoreceptors cell line incubated with  $1.0 \mu\text{g mL}^{-1}$  (Ag content) Ag<sub>2</sub>S NPs dispersion for 24 h. b,c) NIR optical microscopy images. d,h) Bright-field images. e,i) Fluorescence images showing nuclei stained with DAPI. f,j) NIR images showing the emission of Ag<sub>2</sub>S NPs. The superposed images can be seen in (g) and (k).

Figure S6, Supporting Information). The signal intensity in this region is due to the predominant presence of these two protonic interactions resulting in a higher signal intensity. Furthermore, upon increasing the intensity of the spectra, new positive NOESY signals (green and pink circles in Figure 2 aII,bII), corresponding to interactions between the methylene protons of Ag-DCT and the  $\alpha$ -methylene protons adjacent to the amide group of N-PMA, become clearly visible. In the same frequency range, interaction between the methylene protons of N-PMA and the  $\alpha$ -methylene protons of Ag-DCT can also be appreciated. In the spectrum (Figure 2aII), a slight separation between two signals suggests these two interactions, which are depicted in Figure 2c.

Therefore, as depicted in Figure 2c, these experiments show that the aliphatic parts of N-PMA intercalate between the Ag-DCT molecules anchored on the NPs, allowing for the identification of the noncovalent ligand-ligand interactions. This interaction between the aliphatic part of modified-PMA molecules and ligands on NPs surfaces has been previously suggested for other NPs<sup>[31]</sup> but, as far as the authors know, has never been evidenced. Importantly, we believe that the protection conferred by this coverage preserves the optical PL response of the NPs, as shown in Figure 1e. Thus, the successful retention of the initial ligands, without displacement, is a crucial factor in maintaining the PL response. N-PMA effectively intercalates between these retained ligands, as evidenced by NMR, playing a vital role in preventing any significant drop in the PL intensity.

Furthermore, as previously mentioned, N-PMA was employed for magnetic, metallic, and semiconductor NPs, due to its high biocompatibility.<sup>[30–32]</sup> Nevertheless, the corresponding toxicity tests were performed for Ag<sub>2</sub>S NPs treated with N-PMA. Figure 3a shows the results of the cell viability test performed

in the N9 microglia cell line (microglia cells are the resident macrophages of the central nervous system) after a 24 h incubation with the indicated extracellular concentrations of NPs (details can be found in Section S4, Supporting Information). Doses below or equal to  $80 \mu\text{g mL}^{-1}$  (the highest tested) of total extracellular Ag mass, did not affect the viability of the cells (Figure 3a). Additionally, the N9 microglia and the 661 w photoreceptor cell lines were incubated with different concentrations of NP dispersions, ranging from  $4.0$  to  $1.0 \mu\text{g mL}^{-1}$  (Section S4, Supporting Information). N9 cells showed high ability to phagocytose NPs, as shown in the NIR microscopic image in Figure 3b, obtained with a minimum concentration of NPs ( $1.0 \mu\text{g mL}^{-1}$ ). We also found internalization of NPs by the 661 w cells at  $1.0 \mu\text{g mL}^{-1}$ . However, as expected, this cell line was not as effective as the N9 cells at the same concentration (Figure 3c). Figure 3d,h are bright-field images of cells stained with DAPI. The corresponding fluorescence images can be seen in Figure 3e,i. The DAPI-labeled nuclei (see Section S4, Supporting Information for details) showed the cytoplasmic localization of the NPs (Figure 3e–g,i–k). Figure 3f,j correspond to NIR images to localize the presence of Ag<sub>2</sub>S NPs. Figure 3g,k are overlapped images from DAPI and Ag<sub>2</sub>S NPs.

## 2.2. Ag<sub>2</sub>S as Dual OCT Contrast Agents and NIR Probes in Explanted Fixed Eyes

The above-mentioned ensembles have an interesting property that has not been exploited up to now: A strong scattering coefficient. However, due to the small size of individual NPs ( $\approx 7$  nm), the extinction spectrum of isolated Ag<sub>2</sub>S NPs is mainly dominated by absorption,<sup>[38]</sup> which makes them unsuitable as

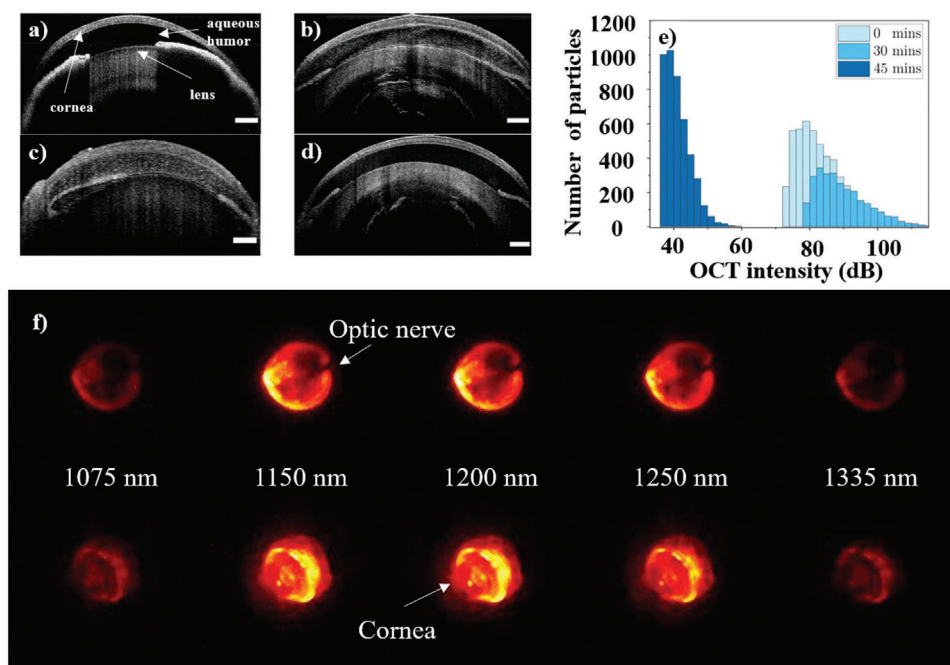


**Figure 4.** Dual OCT-NIR imaging in explanted eyes. OCT images of explanted eyeballs in which 2  $\mu\text{L}$  of a) water and the same volume of  $\text{Ag}_2\text{S}$  NPs dispersion sonicated for b) 0-min, c) 30-min, and d) 45-min had been intravitreally injected. Scale bars correspond to 250  $\mu\text{m}$ . e) OCT intensities distribution for each of the cases in (b–d). f) NIR images of two eyes where 2  $\mu\text{L}$  of  $\text{Ag}_2\text{S}$  NPs ensembles (45-min sonicated) at Ag concentration of 0.8  $\text{mg mL}^{-1}$  had been intravitreally injected. The images in the upper row correspond to an eye where the optical nerve can be inferred. The lower row corresponds to an eye where the cornea and lens are discernible. The images were extracted from a hypercube acquired from 1000 to 1600 nm. Power density: 50  $\text{mW cm}^{-2}$  (0.975 W), exposure time 0.05 s.

contrast agents for techniques based on light scattering such as OCT. But, since the scattering of light strongly depends on the size of the particles, the existence of ensembles of NPs enhances their scattering, making them ideal for OCT. Therefore, the size of the ensembles shown in the previous section can be used to optimize the OCT contrast. This aspect was evidenced by comparing the OCT images of the ensembles obtained after different sonication times at different concentrations, by employing a spectral domain (SD) OCT, with a working wavelength centered at 1300 nm (see Section S5, Supporting Information). Figure S7, Supporting Information demonstrates that  $\text{Ag}_2\text{S}$  ensembles can be visualized clearly by OCT, and that the highest contrast is obtained for larger ensembles according to DLS, as expected.

To explore the OCT contrast provided by the ensembles once they are introduced in an organ, we analyzed fixed, explanted eyeballs (see Section S5, Supporting Information, for details). Figure 4 shows the B-scans of eyes in which 2  $\mu\text{L}$  of a dispersion of  $\text{Ag}_2\text{S}$  NPs ensembles (samples 0-, 30- and 45-min sonicated, see Figure 1) were injected intravitreally, together with a control eye in which 2  $\mu\text{L}$  of ultrapure water (vehicle) was injected. The Ag concentrations (measured by ICP-OES) of the samples were 1.0, 0.6, and 1.3  $\text{mg mL}^{-1}$  for the 0-, 30- and 45-min sonicated samples, respectively. The presence of the NPs is evidenced by the bright spots that appear in the aqueous humor (region between the cornea and the lens) which were absent in the control eye (Figure 4a). All the tested samples increased contrast, although the contrast level offered by the 45-min sonicated samples was lower (even at higher concentrations) than that of the 0- and 30-min sonicated ones, (Figure 4b–d), in good agreement with

the size provided by DLS (see Figure 1c). This is illustrated in the histogram of the intensity of the bright spots that appear in the aqueous humor (Figure 4e) which shows the correlation between the OCT intensity and the sizes of the ensembles provided by DLS. Figure 4f shows NIR PL of 2 explanted eyeballs injected with 2  $\mu\text{L}$  of  $\text{Ag}_2\text{S}$  NPs ensembles (45-min sonicated) at a Ag concentration of 0.8  $\text{mg mL}^{-1}$  from different positions, to show the back and the front parts of the eye.

The images were acquired with a hyperspectral imager (see Section S6, Supporting Information), from which several images at characteristic wavelengths have been extracted and presented here. The brightest images correspond to the 1150 nm wavelength, in good agreement with the maximum in the PL response. In addition, the brightness provided by the NPs allows identifying features of the eye morphology such as the optic nerve (upper series) and the lens/corneal front part (lower series) with high resolution. Therefore, these images demonstrate the multi-imaging role of  $\text{Ag}_2\text{S}$  NPs ensembles as both an OCT contrast agent and a NIR ocular imaging probe in explanted eyes.

### 2.3. $\text{Ag}_2\text{S}$ as Dual OCT Contrast Agents and NIR Probes In Vivo

Building on the promising ex vivo results shown above (presented in Figure 4), we conducted further testing to evaluate the potential of  $\text{Ag}_2\text{S}$  ensembles as contrast agents for ophthalmological OCT. To this aim, we administered the  $\text{Ag}_2\text{S}$  NPs samples used in Figure 4b–d to CD1 mice by intravitreal injection, and images of the eye fundus (reflectance) were acquired by using a

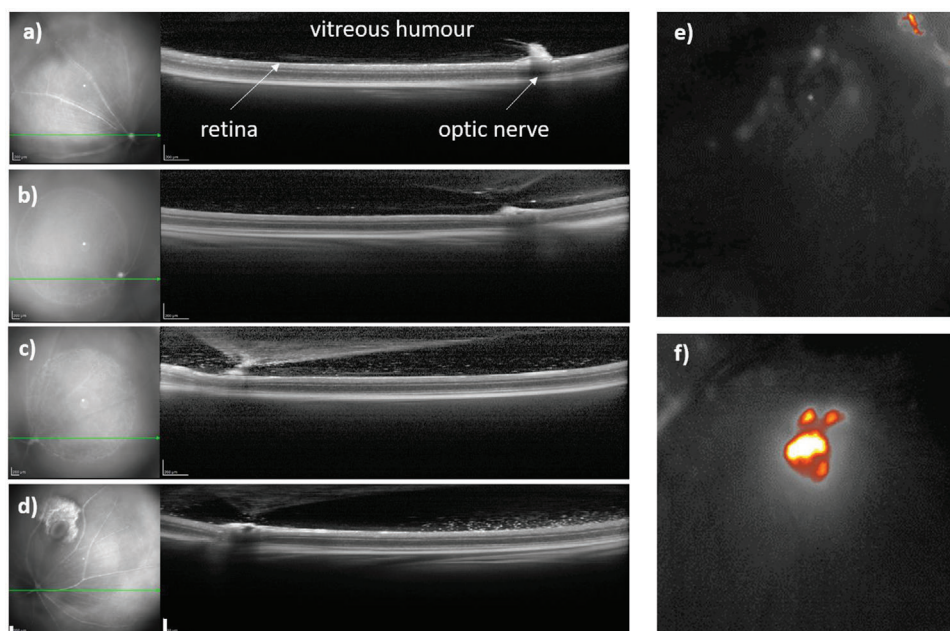


**Figure 5.** OCT imaging in vivo. a–d) Left, NIR images depicting the eye fundus image with indicated orientation of cross-sectional SD-OCT scans (green line) and their corresponding B-scan at the optic nerve level for the eyes injected with 1  $\mu\text{L}$  of water [a) control], b) 45-min, c) 30-min, and d) 0-min sonicated  $\text{Ag}_2\text{S}$  ensembles. e, f) Fluorescence images showing the fluorescence of a mouse eye intravitreally injected with 1  $\mu\text{L}$  of e) PBS and f) a 45-min sonicated sample (at a  $\text{Ag}$  concentration of  $0.9 \text{ mg mL}^{-1}$ ). The scale bars in the OCT images correspond to  $200 \mu\text{m}$ .

commercially available high-speed SD-OCT operating at a wavelength of  $870 \text{ nm}$  (see Section S5, Supporting Information). This system is commonly used in clinical settings to provide imaging of the vitreoretinal interface and retina in human patients.

**Figure 5** shows representative OCT images obtained in vivo from control mouse eyes injected with  $1 \mu\text{L}$  of vehicle (ultrapure water) (Figure 5a) and eyes injected with  $1 \mu\text{L}$  of the NP dispersions, corresponding to the 45-, 30-, and 0-min sonicated samples (Figure 5b–d). The left panels show the corresponding NIR reflectance images of the eye fundus while the right panels show B-scans that present a 2D image of the retina obtained by accumulating 100 scans at the optic nerve level (green line depicted in the fundus reflectance image). The fundus images show the main vascular structures of the inner retina. The vitreous humor of all eyes treated with NPs exhibits a clear brightness increment when compared to the control eye injected with water (Figure 5a). In particular, eyes injected with 30- or 0-min sonicated NPs show clear accumulation of bright spots in the vitreous, which were absent in control eyes and can be attributed to the presence of the  $\text{Ag}_2\text{S}$  NPs ensembles. Differences in the density of spots, on the other hand, can be attributed to variations in injection efficiency or differences in the initial concentration of NP dispersions.

Additionally, the distribution of the NPs in the vitreous was also studied by performing consecutive B-scans at different retinal levels of the fundus in relation to the optic nerve (central retina) and to the injection direction (dorsotemporal retina) (see Figure S8, Supporting Information). The results evidence that the amount of NP ensembles was higher in the retinal section close to the optical nerve level. This observation has been previously reported in other works where polymeric nanocarriers were intravitreally injected.<sup>[39,40]</sup> Furthermore, the size and charge of

the carriers play also a pivotal role in the localization of particles, showing concentration gradients or accumulation in the optical nerve as a result of convection forces.<sup>[41]</sup> However, the precise location of the NPs after injection needs further study, as a more homogeneous distribution of NPs throughout the entire volume of the eyeball may also occur, as it can be seen in Figure S9, Supporting Information. The dual performance of  $\text{Ag}_2\text{S}$  NPs was also tested in vivo (Figure 5e,f), which shows the PL images of the eyes of mice after intravitreal injection with  $1 \mu\text{L}$  of PBS and with  $1 \mu\text{L}$  of a  $\text{Ag}_2\text{S}$  NP ensembles (a 45-min sonicated sample at a  $\text{Ag}$  concentration of  $0.9 \text{ mg mL}^{-1}$ ), respectively. While no PL signal could be acquired from the eye without NPs (Figure 5e), a strong signal was recorded for the eye with NPs (Figure 5f). This eye showed a clear PL signal between  $900$  and  $1600 \text{ nm}$ , whose maximum intensity is recorded at  $1150 \text{ nm}$  (Figure 5f), demonstrating that the  $\text{Ag}_2\text{S}$  ensembles are excellent multimodal OCT and fluorescent contrast agents. The distribution of NPs in the eye was followed up to  $18 \text{ h}$  after injection (Figure S9, Supporting Information) by fluorescence imaging (see Section S6, Supporting Information). The NIR signal was still clearly visible at  $18 \text{ h}$  after injection, showing that the NPs can be used for relatively long times after administration. During this time, the animals showed no signs of distress nor did the eyes present any morphological differences compared to the control eyes injected with vehicle, which is a good indication of the biocompatibility of the nanomaterial and is in good agreement with previous studies that demonstrate that  $\text{Ag}_2\text{S}$ -based NPs do not show significant in vivo toxicity for up to  $1 \text{ month}$  after administration.<sup>[42]</sup> The elimination pathways of the particles were studied after systemic administration of the particles. The infrared images presented in Figure S10, Supporting Information show that in the first minute



after particle administration, Ag<sub>2</sub>S allows visualization of the mouse vascular system (Figure S10b, Supporting Information), although the volume of NP injected (50  $\mu$ L, Ag concentration 0.9 mg mL<sup>-1</sup>) is lower than the one previously employed in these experiments.<sup>[3,8]</sup> Some initial accumulation of the Ag<sub>2</sub>S ensembles was observed in the pulmonary area (a phenomenon frequently observed due to the small size of the pulmonary capillaries) (Figure S10a,b, Supporting Information), but after some minutes the accumulation is reduced. Ex vivo analysis of the organ's luminescence, obtained with a hyperspectral imager, revealed that after 2 h the NPs have accumulated mainly in the liver and the spleen, and only a residual signal can be observed in the lungs (Figure S10c–f, Supporting Information), showing that the fate of the NPs ensembles, once they reach the circulatory system, does not differ from that reported in previous works, which supports their suitability for in vivo imaging.<sup>[3]</sup>

### 3. Conclusions

Ag<sub>2</sub>S NPs can act both as OCT contrast agents and NIR imaging probes, when controlled ensembles of the emitting NPs are obtained. For this purpose, in this work, we have developed a procedure that includes the use of N-PMA, a copolymer that confers biocompatibility and colloidal stability. Due to the interaction of this copolymer with the ligands that passivate the surface of the Ag<sub>2</sub>S NPs, the PL of the NPs is retained, allowing high-resolution NIR imaging. The use of dual OCT-PL probes allows improving NIR imaging depth and OCT contrast, opening promising avenues for ocular imaging.

### Statistics Announcement

Data presentation in Figure 3a corresponds to mean  $\pm$  SD,  $n = 3$ .

### Supporting Information

Supporting Information is available from the Wiley Online Library or from the author.

### Acknowledgements

This work was funded by the Ministry of Science and Innovation (Spain) through the projects PID2020-118878RB-I00, PID2019-106211RB-I00, PID2019-109506RB-I00, PID2021-127033OB-C21, and PID2019-108854RA-I00. A.E. acknowledges RYC2020-029282-I contract and R.L.-M. acknowledges FPI PRE2020-96246. Additional funding was provided by the Instituto de Salud Carlos III (PI19/00565), by the Comunidad Autónoma de Madrid (CAM) and the Universidad Autónoma de Madrid (SI3-PJI-2021-00211), the CAM (S2022/BMD-7403 RENIM-CM) co-financed by the European structural and investment fund, and through COST action CA17140, supported by COST (European Cooperation in Science and Technology), as well as the Fundación para la Investigación Biomédica del Hospital Universitario Ramón y Cajal program IMP21\_A4 (2021/0427). A.C. acknowledges the JAE-Intro grant from the Nanomedicine Hub CSIC. Mice were housed and handled in accordance with the ARVO statement for the Use of Animals in Ophthalmic and Vision Research and the guidelines of the European Union and the local ethics committees of the CSIC and the Comunidad de Madrid (Ref: PROEX 272.8/21, 01 October 2021).

### Conflict of Interest

The authors declare no conflict of interest.

### Data Availability Statement

The data that support the findings of this study are available from the corresponding author upon reasonable request.

### Keywords

fluorescence imaging, multimodal contrast agents, optical coherence tomography, silver sulphide nanoparticles

Received: June 15, 2023

Revised: July 23, 2023

Published online: August 18, 2023

- [1] Y. Shen, J. Lifante, E. Ximendes, H. D. A. Santos, D. Ruiz, B. H. Juárez, I. Zabala Gutiérrez, V. Torres Vera, J. Rubio Retama, E. Martín Rodríguez, D. H. Ortigies, D. Jaque, A. Benayas, B. del Rosal, *Nanoscale* **2019**, *11*, 19251.
- [2] Y. Zhang, Y. Liu, C. Li, X. Chen, Q. Wang, *J. Phys. Chem. C* **2014**, *118*, 4918.
- [3] H. D. A. Santos, I. Zabala Gutiérrez, Y. Shen, J. Lifante, E. Ximendes, M. Laurenti, D. Méndez-González, S. Melle, O. G. Calderón, E. López Cabarcos, N. Fernández, I. Chaves-Coira, D. Lucena-Agell, L. Monge, M. D. Mackenzie, J. Marqués-Hueso, C. M. S. Jones, C. Jacinto, B. del Rosal, A. K. Kar, J. Rubio-Retama, D. Jaque, *Nat. Commun.* **2020**, *11*, 2933.
- [4] C. Li, L. Cao, Y. Zhang, P. Yi, M. Wang, B. Tan, Z. Deng, D. Wu, Q. Wang, *Small* **2015**, *11*, 4517.
- [5] E. Navarro Cerón, B. del Rosal, F. Ren, A. Benayas, F. Vetrone, D. Ma, F. Sanz-Rodríguez, J. G. Solé, D. Jaque, E. Martín Rodríguez, *Adv. Mater.* **2015**, *27*, 4781.
- [6] H. Chen, B. Li, M. Zhang, K. Sun, Y. Wang, K. Peng, M. Ao, Y. Guo, Y. Gu, *Nanoscale* **2014**, *6*, 12580.
- [7] S. Mateos, J. Lifante, C. Li, E. C. Ximendes, T. Muñoz-Ortiz, J. Yao, M. Fuente-Fernández, Á. L. García Villalón, M. Granado, I. Zabala Gutierrez, J. Rubio-Retama, D. Jaque, D. H. Ortigies, N. Fernández, *Small* **2020**, *16*, 1907171.
- [8] D. H. Ortigies, Á. L. García-Villalón, M. Granado, S. Amor, E. M. Rodríguez, H. D. A. Santos, J. Yao, J. Rubio-Retama, D. Jaque, *Nano Res.* **2019**, *12*, 749.
- [9] B. del Rosal, D. Ruiz, I. Chaves-Coira, B. H. Juárez, L. Monge, G. Hong, N. Fernández, D. Jaque, *Adv. Funct. Mater.* **2018**, *28*, 1806088.
- [10] J. Lifante, Y. Shen, I. Zabala Gutierrez, I. Rubia-Rodríguez, D. Ortega, N. Fernandez, S. Melle, M. Granado, J. Rubio-Retama, D. Jaque, E. Ximendes, *Adv. Sci.* **2021**, *8*, 2003838.
- [11] E. Ximendes, R. Marin, Y. Shen, D. Ruiz, D. Gómez-Cerezo, P. Rodríguez-Sevilla, J. Lifante, P. X. Viveros-Méndez, F. Gámez, D. García-Soriano, G. Salas, C. Zalbidea, A. Espinosa, A. Benayas, N. García-Carrillo, L. Cussó, M. Desco, F. J. Teran, B. H. Juárez, D. Jaque, *Adv. Mater.* **2021**, *33*, 2100077.
- [12] Y. Du, B. Xu, T. Fu, M. Cai, F. Li, Y. Zhang, Q. Wang, *J. Am. Chem. Soc.* **2010**, *132*, 1470.
- [13] H. Doh, S. Hwang, S. Kim, *Chem. Mater.* **2016**, *28*, 8123.
- [14] P. Jiang, Z.-Q. Tian, C.-N. Zhu, Z.-L. Zhang, D.-W. Pang, *Chem. Mater.* **2012**, *24*, 3.
- [15] A. Sahu, L. Qi, M. S. Kang, D. Deng, D. J. Norris, *J. Am. Chem. Soc.* **2011**, *133*, 6509.



- [16] H. Zhang, B.-R. Hyun, F. W. Wise, R. D. Robinson, *Nano Lett.* **2012**, 12, 5856.
- [17] G. Zhu, Z. Xu, *J. Am. Chem. Soc.* **2011**, 133, 148.
- [18] D. Ruiz, M. Mizrahi, H. D. A. Santos, D. Jaque, C. M. S. Jones, J. Marqués-Hueso, C. Jacinto, F. G. Requejo, A. Torres-Pardo, J. M. González-Calbet, B. H. Juárez, *Nanoscale* **2019**, 11, 9194.
- [19] I. Z. Gutierrez, C. Gerke, Y. Shen, E. Ximendes, M. M. Silvan, R. Marin, D. Jaque, O. G. Calderón, S. Melle, J. Rubio-Retama, *ACS Appl. Mater. Interfaces* **2022**, 14, 4871.
- [20] T. Muñoz-Ortiz, R. Marin, D. H. Ortgies, E. M. Rodríguez, *J. García Solé*, **2022**, 5, 371.
- [21] V. P. Nguyen, W. Qian, X. Wang, Y. M. Paulus, *Methods Enzymol.* **2021**, 657, 443.
- [22] J. Hu, D. Romero Abujetas, D. Tsoutsis, L. Leggio, F. Rivero, E. Martín Rodríguez, R. Aguilar Torres, J. A. Sánchez-Gil, H. Loro Ramírez, D. Gallego, H. Lamela Rivera, P. Rivera Gil, F. Alfonso, J. García Solé, D. Jaque, *APL Photonics* **2018**, 3, 080803.
- [23] S. Shah, C.-N. Yu, M. Zheng, H. Kim, M. S. Eggleston, *ACS Nano* **2021**, 15, 9764.
- [24] R. Marin, J. Lifante, L. V. Besteiro, Z. Wang, A. O. Govorov, F. Rivero, F. Alfonso, F. Sanz-Rodríguez, D. Jaque, *Adv. Healthcare Mater.* **2020**, 9, 1901627.
- [25] J. Hu, D. H. Ortgies, R. Aguilar Torres, N. Fernández, L. Porto, E. Martín Rodríguez, J. García Solé, D. Jaque, F. Alfonso, F. Rivero, R. Aguilar Torres, N. Fernández, L. Porto, E. Martín Rodríguez, J. García Solé, D. Jaque, F. Alfonso, F. Rivero, *Adv. Funct. Mater.* **2017**, 27, 1703276.
- [26] J. Yao, T. Muñoz-Ortiz, F. Sanz-Rodríguez, E. Martín Rodríguez, D. H. Ortgies, J. García Solé, D. Jaque, R. Marin, *ACS Photonics* **2022**, 9, 559.
- [27] G. Sukkarieh, R. Lejoyeux, Y. LeMer, S. Bonnin, R. Tadayoni, *Surv. Ophthalmol.* **2023**, 68, 313.
- [28] C. N. Thomas, N. Alfahad, N. Capewell, J. Cowley, E. Hickman, A. Fernandez, N. Harrison, O. S. Qureshi, N. Bennett, N. M. Barnes, A. D. Dick, C. J. Chu, X. Liu, A. K. Denniston, M. Vendrell, L. J. Hill, *Biosens. Bioelectron.* **2022**, 216, 114623.
- [29] N. Erathodiyil, J. Y. Ying, *Acc. Chem. Res.* **2011**, 44, 925.
- [30] F. Zhang, E. Lees, F. Amin, P. RiveraGil, F. Yang, P. Mulvaney, W. J. Parak, *Small* **2011**, 7, 3113.
- [31] T. Pellegrino, L. Manna, S. Kudara, T. Liedl, D. Koktysh, A. L. Rogach, S. Keller, J. Rädler, G. Natile, W. J. Parak, *Nano Lett.* **2004**, 4, 703.
- [32] E. Peng, E. S. G. Choo, Y. Sheng, J. M. Xue, *New J. Chem.* **2013**, 37, 2051.
- [33] W. Wang, A. Kapur, X. Ji, M. Safi, G. Palui, V. Palomo, P. E. Dawson, H. Mattoussi, *J. Am. Chem. Soc.* **2015**, 137, 5438.
- [34] M. G. Soliman, B. Pelaz, W. J. Parak, P. del Pino, *Chem. Mater.* **2015**, 27, 990.
- [35] X. Zhuo, M. Henriksen-Lacey, D. Jimenez de Aberasturi, A. Sánchez-Iglesias, L. M. Liz-Marzán, *Chem. Mater.* **2020**, 32, 5879.
- [36] A. Bera, S. S. Pathak, V. Kotha, B. L. V. Prasad, *Adv. Mater. Interfaces* **2021**, 8, 2100898.
- [37] D. Ruiz, B. del Rosal, M. Acebrón, C. Palencia, C. Sun, J. Cabanillas-González, M. López-Haro, A. B. Hungria, D. Jaque, B. H. Juárez, *Adv. Funct. Mater.* **2017**, 27, 1604629.
- [38] T. A. Estrada-Mendoza, D. Willett, G. Chumanov, *J. Phys. Chem. C* **2020**, 124, 27024.
- [39] V. Junnuthula, A. Sadeghi Boroujeni, S. Cao, S. Tavakoli, R. Ridolfo, E. Toropainen, M. Ruponen, J. C. M. van Hest, A. Urtti, *Pharmaceutics* **2021**, 13, 445.
- [40] J. F. Jordan, I. Semkova, N. Kociok, G. R. Welsandt, G. K. Kriegelstein, U. Schraermeyer, *Graefes Arch. Clin. Exp. Ophthalmol.* **2002**, 240, 403.
- [41] E. M. del Amo, A.-K. Rimpelä, E. Heikkinen, O. K. Kari, E. Ramsay, T. Lajunen, M. Schmitt, L. Pelkonen, M. Bhattacharya, D. Richardson, A. Subrizi, T. Turunen, M. Reinisalo, J. Itkonen, E. Toropainen, M. Casteleijn, H. Kidron, M. Antopolsky, K.-S. Vellonen, M. Ruponen, A. Urtti, *Prog. Retinal Eye Res.* **2017**, 57, 134.
- [42] C. Lu, G. Chen, B. Yu, H. Cong, *Adv. Eng. Mater.* **2018**, 20, 1700940.